Time-independent square patterns in surface-tension-driven Bénard convection

Michael F. Schatz[a)]
School of Physics, Georgia Institute of Technology, Atlanta, Georgia 30332

Stephen J. VanHook, W. D. McCormick, J. B. Swift, and Harry L. Swinney
Center for Nonlinear Dynamics and Department of Physics, The University of Texas at Austin, Austin, Texas 78712

(Received 14 October 1998; accepted 13 May 1999)

The transition between hexagonal and square patterns is investigated in laboratory experiments on surface-tension-driven Bénard (Marangoni) convection in a fluid of Prandtl number 81. As the Marangoni number M is increased, an ideal hexagonal pattern is supplanted by a defect-free square pattern; the transition occurs gradually with patterns of mixed hexagonal, pentagonal, and square symmetry arising at intermediate values of M. An elementary topological process associated with two-dimensional patterns governs local changes in morphology; the dynamics are relaxational with all patterns becoming stationary with M fixed for a sufficiently long time. The transition is hysteretic and depends strongly on the pattern wave number. © *1999 American Institute of Physics.* [S1070-6631(99)00209-3]

I. INTRODUCTION

Hexagonal flow patterns have been associated with the onset of convection ever since Bénard's observations of thin fluid layers heated from below;[1] until recently, however, the transition from hexagons to other patterns was unexplored for the surface-tension-driven regime of Bénard's studies. Experiments with fluids of very high Prandtl number $P \sim 1000$ suggest that defects increase in number with increased heating, thereby inducing a gradual transition from hexagons to disordered cellular arrays that can be characterized using techniques describing melting in two-dimensional (2-D) systems.[2] Alternatively, more recent experiments with $P \sim 100$ demonstrate a transition from hexagons to square patterns as the heating is increased.[3,4] In both cases, the experimental results suggest that time-dependent flows arise from the instability of hexagons.

We report the observation of time-independent square patterns arising from secondary instability in surface-tension-driven Bénard (Marangoni) convection experiments on a fluid with $P=81$. As the temperature gradient across the layer is increased quasistatically, hexagonal patterns lose stability to patterns of mixed symmetry as individual hexagons undergo local changes in topology and transform first into pentagons and, then, into squares; for sufficiently large heating, the system forms a nearly ideal square pattern. For a fixed temperature gradient, these states are time independent, even when the pattern is a mixture of hexagons, pentagons, and squares. The transition between patterns exhibits hysteresis; moreover, the transition onset depends on the pattern wave number, which, in turn, depends on the initial conditions of the experiment.

a)Electronic mail: michael.schatz@physics.gatech.edu

II. DESCRIPTION OF EXPERIMENT

Surface tension gradients at the interface between silicone oil and air layers drive flow patterns in our experiments (Fig. 1). The silicone oil layer is heated from below by a 1 cm thick gold coated aluminum mirror at a temperature T_b; the air layer is cooled from above by a 0.3 cm thick sapphire window at a temperature T_t. For sufficiently small $T_b - T_t$, the oil–air interface is isothermal and the surface tension $\sigma(T)$ is uniform. With $T_b - T_t$ sufficiently large, instability induces surface tension variations at the interface that drive flow in the bulk. The average temperature difference across the oil layer ΔT is related to T_b and T_t as described below; we use ΔT to form the dimensionless parameter, the Marangoni number M, which describes the strength of the surface tension driving: $M \equiv \sigma_T \Delta T d/\rho\nu\kappa$, where $\sigma_T \equiv |d\sigma/dT|$, and ρ, ν, κ are, respectively, the liquid density, kinematic viscosity, and thermal diffusivity (Table I). For heating from below, flow may also be driven by buoyancy as characterized by the Rayleigh number $R \equiv g\alpha\Delta T d^3/\nu\kappa$ with liquid expansion coefficient α and gravitational acceleration g. We minimize buoyancy effects by performing experiments in thin liquid layers where $8 < M/R \equiv \sigma_T/(\rho\alpha g d^2) < 15$ independent of ΔT (Table II). The corresponding Rayleigh number in the air is negligibly small.

During assembly of the convection apparatus, the distance $d + d_g$ (Fig. 1) is set using indium shims that are deformed to a predefined thickness. The mirror and the window are then aligned parallel within ± 2 μm by interferometry. A precisely defined volume of silicone oil is injected into the apparatus to set both d and d_g. (The dependence of d on the oil volume is determined by calibration.) The entire convection apparatus is then adjusted until the liquid surface is aligned parallel with the mirror and window within ± 2 μm, except for a small region in the vicinity of the sidewall, where there is nonuniformity due to irregular pinning of the

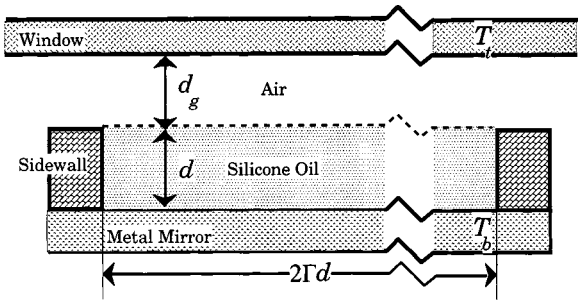

FIG. 1. Cross section of our cylindrical convection apparatus.

meniscus at the sidewall. T_b is imposed by a thin-film heater; during a run T_b fluctuates by $\pm 0.0003\,^{\circ}\mathrm{C}$ about the computer-controlled setpoint values. T_t is fixed by cooling water at $13.310 \pm 0.002\,^{\circ}\mathrm{C}$, which washes over the window and circulates around a chamber that encloses the convection apparatus. The temperature is measured using thermistors placed in the bottom mirror and above the top window. Commercial silicone oils (polydimethylsiloxane) are distilled to eliminate multiple polymer components; the resulting purified oil consists of a single component, hexacosamethyldodecasiloxane, of >95% purity with Prandtl number $P=81$ and other physical properties as listed in Table I.[5] The sidewall is made of Teflon bonded to an aluminum ring that surrounds the mirror.

Patterns are visualized using the shadowgraph method. The images are acquired from a standard NTSC video camera by a computer-controlled frame grabber and by a time-lapse VCR. The patterns are analyzed by representing the images using a Wigner–Seitz construction.[6] A threshold is applied to the images to determine the centers of the cells (the warm upflow regions). The Wigner–Seitz construction is then formed by finding the midpoints of each line segment that joins a cell center to its nearest neighbors; the perpendicular bisectors at the midpoints intersect to form a closed convex polygon that is associated with each cell center. The boundaries of the Wigner–Seitz polygons are seen to faithfully match the downflow boundaries from the shadowgraph images (Fig. 2). We use the Wigner–Seitz representation to determine the relative fraction n and the average area A for cells of a given symmetry. The average wavelength λ is obtained from A, assuming all cells of a given symmetry have edges of equal length; in this case, the average wavelength for squares is $\lambda_s = \sqrt{A_s}$ and the average wavelength for hexagons is $\lambda_h = \sqrt{\sqrt{3}A_h/2}$.

TABLE I. Values at 25 °C of silicone oil and air physical properties for surface-tension-driven Bénard convection experiments.

Oil density ρ	$0.93\ \mathrm{g\,cm^{-3}}$
Oil kinematic viscosity ν	$0.070\ \mathrm{cm^2\,s^{-1}}$
Oil thermal diffusivity κ	$8.6\times10^{-4}\ \mathrm{cm^2\,s^{-1}}$
Oil thermal expansion coeff. α	$1.0\times10^{-3}\ \mathrm{K^{-1}}$
Surface tension coeff. $\lvert d\sigma/dT\rvert$	$0.068\ \mathrm{dyne\,cm^{-1}\,K^{-1}}$
Oil thermal conductivity k	$13.0\times10^{3}\ \mathrm{erg\,s^{-1}\,cm^{-1}\,K^{-1}}$
Air thermal conductivity k_g	$2.6\times10^{3}\ \mathrm{erg\,s^{-1}\,cm^{-1}\,K^{-1}}$

TABLE II. Parameters for the two experimental configurations explored in our surface-tension-driven Bénard convection experiments.

Parameter	Config. 1	Config. 2
Oil depth d (cm)	$7.11\pm0.04\times10^{-2}$	$9.65\pm0.04\times10^{-2}$
Air depth d_g (cm)	$10.39\pm0.04\times10^{-2}$	$7.55\pm0.04\times10^{-2}$
Time scale τ_v (s)	5.9	10.8
Aspect ratio Γ	32	23
Biot number B	0.14	0.26
M/R	15	8

Using an infrared camera in separate experiments, we directly measure the horizontally averaged temperature at the interface $\langle T_i \rangle$ to obtain the temperature difference across the oil layer $\Delta T \equiv T_b - \langle T_i \rangle$ used in our definition of M. We use an infrared detector (liquid nitrogen-cooled 256×256 array of indium antimonide photodiodes) to measure thermal radiation emitted from a silicone oil mixture consisting of approximately 90% commercial polydimethylsiloxane ($0.05\ \mathrm{cm^2\,s^{-1}}$ viscosity) and 10% polymethylhydrosiloxane ($0.35\ \mathrm{cm^2\,s^{-1}}$ viscosity). This blend of silicone oils ensures that the detected thermal radiation is emitted essentially at the surface of the oil (within $\sim 50\ \mu$m of the interface); i.e., the oil layer appears as a nearly ideal blackbody when the detector is narrow bandpass filtered around the very strong absorption peak for polymethylhydrosiloxane at 4.61 μm. The exact mixture ratio of the silicone oils is chosen to match the viscosity at 25 °C of the purified fluids used in the pattern forming experiments (Table I). This mixture is put in a specially built convection apparatus where the window (Fig. 1) is liquid cooled using chloroform, which is transparent to thermal emissions in the range of interest.[7] The imager is first calibrated using a silicone oil layer that is sufficiently thin to remain in the conduction regime for a wide range of temperatures; oil is then added until d and d_g match that of the pattern forming experiments. Thermal images are then captured and used to measure $\langle T_i \rangle$ and, therefore, determine ΔT as a function of $T_b - T_t$. We apply this temperature calibration to our pattern forming experiments, where infrared imaging could not be used by assuming both

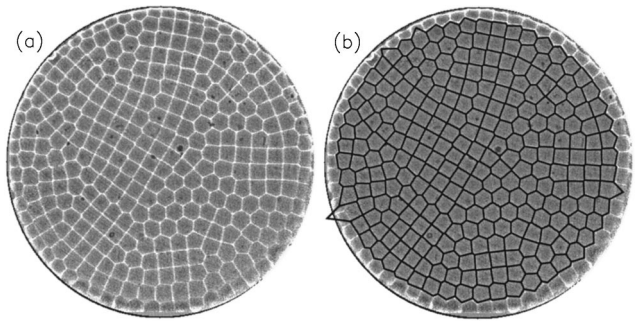

FIG. 2. Patterns obtained from Marangoni convection experiments are well represented using a Wigner–Seitz unit cell construction. A pattern is shown for $d=0.0711$ cm. (a) The pattern planform is visualized using shadowgraphy; warm fluid wells up to the layer's free surface in each cell's center (dark region) and flows back down into the layer at the cooler edges of each cell (bright lines). (b) A Wigner–Seitz construction (black lines) is superimposed on the pattern in the original shadowgraph image shown in (a).

TABLE III. Coefficients for determining the Marangoni number M from temperature calibrations using infrared imaging with measurements of T_b and T_t expressed as $M_{\mathrm{cond}}: M = C_0 + C_1 M_{\mathrm{cond}}$.

d (cm)	C_0	C_1
$7.11 \pm 0.04 \times 10^{-2}$	24.34	0.6536
$9.65 \pm 0.04 \times 10^{-2}$	40.68	0.4900

experiments have the same ΔT for a given $T_b - T_t$; in Table III, this is represented by expressing M ($\propto \Delta T$) as a function of M_{cond} ($\propto T_b - T_t$), the Marangoni number based on $\Delta T_{\mathrm{cond}} \equiv (T_b - T_t) \cdot (1 + B^{-1})^{-1}$ with the Biot number $B \equiv k_g d / k d_g$ (see Fig. 3). Below the onset of convection, B describes the conductive heat transport across the oil–air interface and $\Delta T = \Delta T_{\mathrm{cond}}$. Above onset, however, the convective flow in the oil enhances heat transport relative to pure conduction, so $\Delta T < \Delta T_{\mathrm{cond}}$. Nevertheless, both M and M_{cond} are well-defined control parameters with different advantages for describing flow above the onset of convection. M_{cond} (unlike M) is independent of the flow structure[8] while M permits a comparison to previous experiments,[2] where the air layer is unbounded above and M_{cond} is ill defined. For the results presented here, we use the reduced Marangoni numbers $\epsilon \equiv (M - M_c)/M_c$ and $\epsilon_{\mathrm{cond}} \equiv (M_{\mathrm{cond}} - M_c)/M_c$, where M_c is the critical value of the Marangoni number determined from linear stability theory.[8]

III. EXPERIMENTAL RESULTS

An overview of the transition from hexagons and squares is illustrated in Fig. 4. We investigate the transition by slowly ramping ϵ over a range sufficient to induce changes in the pattern; for our studies $d\epsilon/dt \approx 3 \times 10^{-4}$, where time is scaled by $\tau_v = d^2/\kappa$ (Table II). We typically begin experimental runs at low values of ϵ, where stationary hexagons are stable and cycle the control parameter by quasistatically and repeatedly increasing and decreasing ϵ over some range. Beginning with the onset of convection, a hexagonal pattern with a few nonhexagonal defects arises and persists for a range of ϵ [Fig. 4(a)]. As ϵ is increased further, some hexagons transform into pentagons and squares [Fig. 4(b)]. With ϵ sufficiently large, the pattern exhibits mostly square cells, with nonsquare cells limited to the periphery of the apparatus to accommodate the pattern within the circular lateral boundary [Fig. 4(c)]. In this range of ϵ, the interior of the pattern sometimes consists of a single domain of squares, as shown in Fig. 4(c), or may contain multiple (typically two or three) domains with differing orientation of the square pattern; the selection between square patterns of either single or multiple domains depends on the initial conditions of the experiment. As ϵ is then decreased, the square pattern loses stability; patterns of mixed symmetry like in Fig. 4(b) reappear; a planform dominated by hexagonal cells reappears with ϵ sufficiently small [Fig. 4(d)].

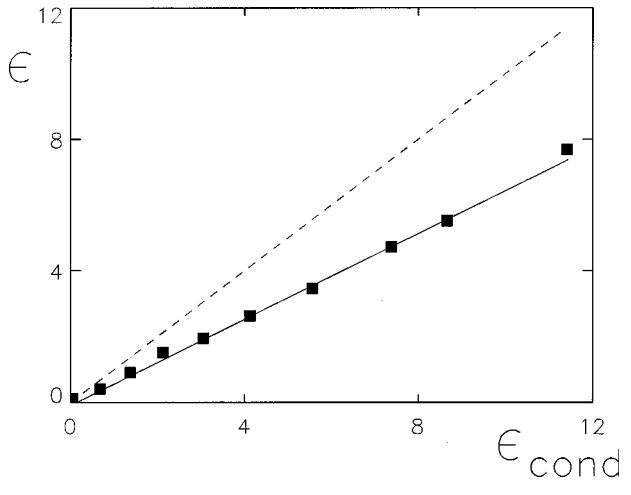

FIG. 3. A calibration curve for determining the reduced Marangoni number ϵ for $d = 0.0711$ cm. For each data point (solid squares), ϵ_{cond} is determined from T_t and T_b, assuming conductive heat transport, while ϵ is determined from a direct measurement by infrared imaging of the average temperature at the liquid–gas interface. The solid line represents a linear least-squares fit to the data; the dashed line corresponds to $\epsilon = \epsilon_{\mathrm{cond}}$.

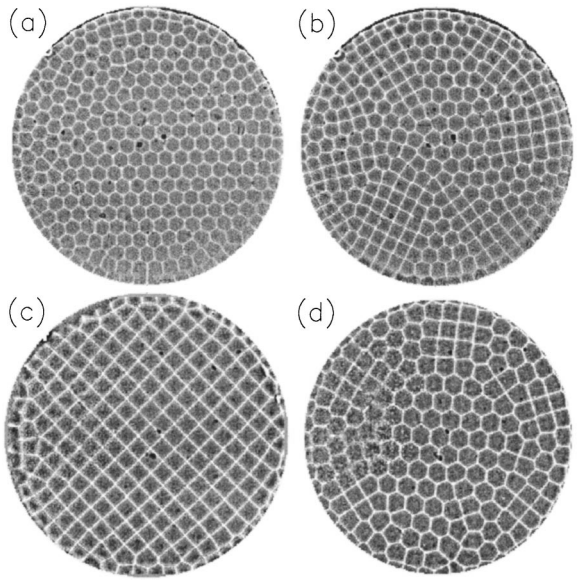

FIG. 4. Shadowgraph images illustrate the secondary instability leading to square patterns in Marangoni convection with $d = 0.0711$ cm. The convective pattern changes with increasing ϵ from hexagons at $\epsilon = 1.61$ (a), through a mixed state at $\epsilon = 3.90$ (b), to a square pattern at $\epsilon = 7.22$ (c). As ϵ is then decreased, hexagons reappear in the pattern by $\epsilon = 3.50$ (d); note, however, that the reappearing hexagons are larger than in (a) (see the text). For fixed ϵ, all the patterns are time independent.

Further insight into the transition can be obtained by describing the change to a localized region of the pattern in terms of elementary topological processes by which two-dimensional patterns may be modified. For each convection cell in a hexagonal pattern, downflow boundaries form the six edges of each cell and three edges intersect to form a vertex [Fig. 5(a)]. The topology of hexagonal networks can be modified when an edge shrinks to zero length and the two vertices that terminate the edge approach one another and coalesce to form the intersection of four edges. [Compare, for example, the left edge of cell number 4 in Figs. 5(a)–5(d).] In many hexagonal networks, the four edges will ''swap neighbors'' as the intersection of the four edges splits up into two new vertices that are separated by a new edge;

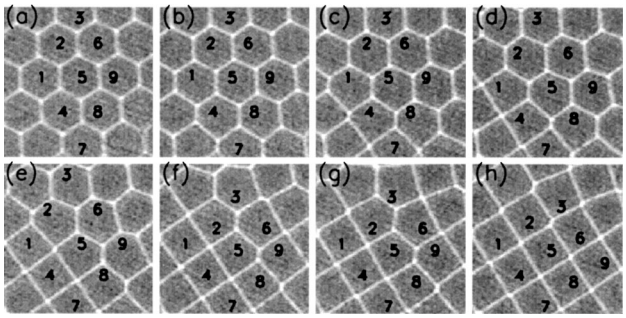

FIG. 5. The transition from hexagons to squares for a localized region of the pattern with increasing ϵ is shown by a sequence of shadowgraph images. Initially, the pattern is a nearly perfect hexagonal lattice at $\epsilon=1.61$ (a) [the lower right corner in Fig. 4(a)]. Cell edges then disappear via an elementary topological process (a modified T1 process; see the text) as ϵ is increased; (b) $\epsilon=2.68$, (c) $\epsilon=2.98$, (d) $\epsilon=3.30$, (e) $\epsilon=3.89$, (f) $\epsilon=4.15$, (g) $\epsilon=4.28$. Eventually, all cells (locally) become squares (h) $\epsilon=4.56$.

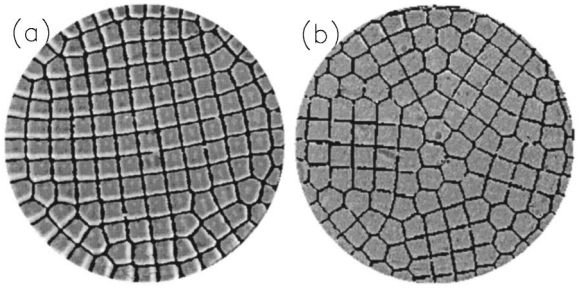

FIG. 6. The very weak time dependence of the patterns is illustrated by superimposed images of the convective flow with $d=0.0965$ cm. (a) Two images of stationary square patterns separated by $54\tau_h$ (almost four days) are shown for $\epsilon=6.0$. The downflow boundaries of the initial pattern and the final pattern are shown in white and black, respectively. (b) Two images of stationary patterns of mixed symmetry separated by $15\tau_h$ (26 h) are shown for $\epsilon=4.5$.

this topological transformation is known as a ''T1 process.''[9] However, for hexagonal patterns with increasing ϵ in Marangoni convection, this T1 process is arrested; as the vertices coalesce, the angles between adjacent edges changes from 120° to 90° and the intersection of four edges becomes stable. Each such arrested T1 process causes two cells to lose an edge; thus, this process initially leads to the formation of pentagons [e.g., cells 1 and 4 in Fig. 5(d)]; with increasing ϵ, further arrested T1 processes lead to the formation of squares [Figs. 5(e)–5(g)]. The occurrence of this process in a given cell tends to induce it in neighboring cells; thus, the formation of vertices with four-fold coordination occurs in chains [e.g., the left and right edges of cells 4 and 7 in Figs. 5(c)–5(f)]. Moreover, distorted cells near the boundary tend to induce this process; thus, pentagons and squares frequently first appear near the lateral boundaries of the pattern. By this process, square cells become predominant as most vertices become fourfold [Fig. 5(h)] with ϵ sufficiently large. As ϵ is decreased, the time-reversed version of this arrested T1 process occurs as fourfold vertices split into two threefold vertices with the appearance of a new edge; this, in turn, leads to the formation of pentagons from squares and, then, hexagons from pentagons. The hexagonal planform returns for ϵ sufficiently small.

All patterns are time independent for fixed conditions in the range of ϵ we explored (Fig. 6). Qualitatively, the time evolution of pattern topology behaves in a relaxational ''stick-slip'' or ''avalanche'' fashion as ϵ is slowly ramped—time periods of no pattern activity are interspersed with periods when one or several arrested T1 processes occur in bursts lasting several tens of τ_v. If the ramping of ϵ is halted at any stage in the transition between the two ideal planforms [Figs. 4(a) and 4(c)], then the pattern may undergo significant changes within $\approx 200\tau_v$ after the ramping of ϵ ceases; thereafter, the patterns typically remain static. In terms of the horizontal diffusion time $\tau_h \equiv \Gamma^2 \tau_v = 1.7$ h, we have observed steady square patterns for fixed ϵ for as long as $54\tau_h$ (almost four days) and steady mixed patterns for as long as $15\tau_h$ (26 h); in both cases, the observation periods were limited only because ϵ was changed to new parameter values (Fig. 6). The observation of stationary patterns depends crucially on the lateral sidewall boundary conditions; in experiments where a nonuniformity in temperature or pinning is known to exist, we observe that cells at the lateral sidewall may move parallel to the boundary and induce motion throughout the entire pattern. Even in well-controlled experiments, small changes in the patterns under fixed conditions can often be attributed to motion of the cells at the lateral boundary [e.g., the slight shifting of cells on the left side of Fig. 6(a)].

The transition between hexagons and squares depends strongly on the initial conditions and the previous history of the pattern. We first consider the case where ϵ is increased up to a value where square cells are just beginning to dominate, i.e., the relative number fraction of square cells n_s has just exceeded $\frac{1}{2}$ [Figs. 4(b) and 7]. The transition appears to be subcritical since the number fraction exhibits hysteresis; a

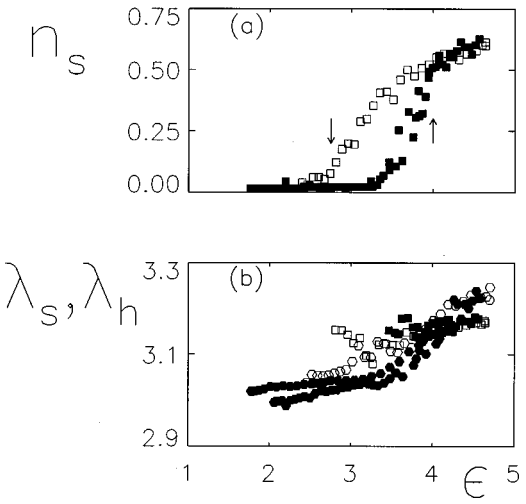

FIG. 7. The relative fraction of squares n_s (a) and wavelength λ of squares and hexagons (b) as a function of ϵ for transition between small hexagons and squares for $d=0.0711$ cm [Figs. 4(a) and 4(b)]. Closed symbols correspond to increasing ϵ quasistatically while open symbols correspond to decreasing ϵ quasistatically; symbol shape indicates cell symmetry. (a) With two complete cycles of increasing and decreasing ϵ, n_s exhibits a repeatable hysteresis loop. (b) The average wavelengths of both hexagons (λ_h) and squares (λ_s) are nearly identical, are reproducible for each cycle, and increase with increasing ϵ. The wavelengths are nondimensionalized by d; for comparison, $\lambda=3.14$ at the onset of hexagonal convection.

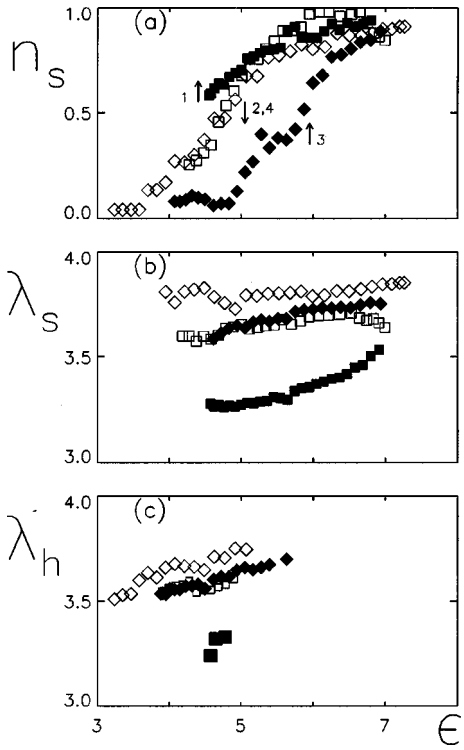

FIG. 8. Relative fraction of squares n_s (a) and wavelength λ of squares (b) and hexagons (c) as a function of ϵ for transition between large hexagons and squares for $d=0.0711$ cm. (a) The beginning with a mixed pattern of small cells [Fig. 4(b)]; ϵ is increased until large squares arise [Fig. 4(c)] (closed squares, up arrow 1). These square patterns lose stability to large hexagons (open squares, down arrow 2) with decreasing ϵ. Subsequent increases in ϵ (closed diamonds, up arrow 3) and decreases in ϵ (open diamonds, down arrow 4) lead to transitions between large hexagons and squares for the range of ϵ shown. (b) Wavelength for squares in the range of ϵ corresponding to the ramps in ϵ in (a). (c) Wavelength for hexagons in the range of ϵ corresponding to the ramps in ϵ described in (a).

substantial number of squares occurs at lower values of ϵ for decreasing ϵ as compared to increasing ϵ [Fig. 4(a)]. Defining the transition to occur at ϵ_s corresponding to $n_s=0.5$ for the pattern, we have $\epsilon_s \approx 3.8$. The wavelengths λ for both hexagons and squares are nearly equal and increase with increasing ϵ [Fig. 4(b)]. In this range of ϵ it is noteworthy that the wavelength's dependence on ϵ is ''reversible;'' the wavelength for both squares and hexagons takes on a unique value as ϵ is cycled and displays little evidence of hysteresis that is present for n_s.

Both n_s and λ exhibit different behavior if the range of ϵ is increased so that the experiment obtains a nearly perfect pattern of squares [Figs. 4(c) and 8]. In this regime, experiments begin also with a pattern of hexagons like in Fig. 4(a); however, instead of decreasing ϵ after n_s just exceeds 0.5, as in Fig. 7, ϵ is further increased until n_s approaches unity [ramp 1 in Fig. 8(a)]. The wavelength for square patterns is observed to increase significantly [Fig. 8(b)] in this process; the increase in square size is readily visible by comparing Figs. 4(b) and 4(c). If ϵ is then decreased [ramp 2 in Fig. 8(a)], n_s exhibits seemingly little hysteresis as squares lose stability to hexagons; however, the square wavelength maintains its increased value [Fig. 8(b)] and induces hexagons with a substantially increased wavelength [Fig. 8(c)], as can be seen by comparing Figs. 4(a) and 4(d). Thereafter, repeated cycling of ϵ (ramps 3 and 4 in Fig. 8) causes the pattern to range between large squares and large hexagons [Figs. 4(c) and 4(d)] with approximately the same wavelength; the transition once again exhibits hysteresis in n_s, with an onset that has increased to $\epsilon_s \approx 5$. The pattern may be returned to a transition like that observed in Fig. 7 by decreasing ϵ to sufficiently small values such that a pattern of small hexagons returns.

IV. COMPARISON WITH PREVIOUS WORK

Our results support several findings of the experiments of Eckert (née Nitschke) and Thess[3] (ET), the numerical simulations of Bestehorn[10] (B), and the combined experiments and simulations of Eckert, Bestehorn and Thess[4] (EBT). ET, B, and EBT find that hexagonal patterns lose stability to square patterns for ϵ sufficiently large. Both ET and EBT observed the transition to squares to appear gradually over a range of ϵ and describe the transition between hexagons and squares as being ''mediated'' by pentagons. ET and EBT also observe hysteresis in the relative number fraction of square cells as ϵ is cycled over the transition range. The simulations of B suggest that the observation of squares requires P to be not too large; this may explain why our observations at $P=81$ and those of ET and EBT at $P=100$ differ from observations of a disordering transition in experiments at $P \approx 1000$.[2]

The time independence of the patterns we observe differs from the experimental observations of EBT, but in agreement with the simulations of EBT. After hexagons lose stability, the experiments of EBT at $P=100$ and $\Gamma=32$ exhibit patterns that continually evolve over slow time scales $\sim \tau_h$; this evolution occurs even for patterns with $n_s=0.55$, the largest relative fraction of squares observed in their experiments. The simulations of EBT at $\Gamma=11.5$, however, suggest that both square and mixed patterns are time independent for $P>40$. EBT suggest that larger Γ in the experiments yields mean flow effects that are sufficiently strong to drive time-dependent flow; however, our experimental results at comparable Γ suggest that the mean flow effects are not sufficiently strong to induce time dependence. Buoyant effects are stronger in the experiments of EBT and may account for the differences in observations; thicker d in EBT yield $M/R \approx 3$, smaller than in our experiments (Table II), while the simulations of EBT neglect buoyancy. Finally, our observations of time dependence induced by the motion of cells near the lateral boundary suggest that nonuniformity at the lateral boundary could drive cell motion in the experiments of EBT, which, in turn, may induce time dependence throughout the entire pattern. Future simulations at large M/R and large Γ should shed some light on this issue.

The results of ET and EBT suggest a well-defined mean ϵ and λ for the appearance of square patterns while our results show that the transition is strongly dependent on the history of the pattern. The experimental results of EBT are consistent with a transition like that shown in Fig. 7, where the pattern ranges between a nearly perfect hexagonal array at low ϵ and a mixed symmetry planform with squares in the bare majority (n_s slightly larger than 0.5) at high ϵ. In this

regime, both our experiments and EBT experiments show that λ of both hexagonal and square cells increase with increasing ϵ; moreover, $\lambda(\epsilon)$ exhibits virtually no hysteresis. However, for transitions where n_s approaches unity, we observe both λ and n_s can exhibit hysteresis and the onset of squares at $n_s=0.5$ is shifted to larger values of ϵ. The simulations of EBT do not address the effect of λ on the transition between hexagons and squares (λ is fixed by the periodic boundary conditions of the simulation). However, the simulations of EBT find that the transition is dependent on Prandtl number P; they estimate that the transition occurs at $\epsilon_{\mathrm{cond}}=0.28P^{0.68}$; for $P=81$ of our experiments, the simulations predict transition at $\epsilon_{\mathrm{cond}}=5.6$, which lies in the range of $4.5<\epsilon_{\mathrm{cond}}<6.4$ observed in our experiments. It should be noted that the simulations of EBT are conducted with $B=0.6$, larger than for our experiments $B=0.14$ or 0.26; moreover, for $d/d_g\approx 1$ of our experiments, it is known that the heat transfer across the oil–air interface at the onset of convection is more sensitive to λ than for the $d/d_g\approx 0.3$ of both experiments and simulations of EBT.[8]

V. CONCLUSIONS

The secondary instability leading to stationary defect-free square patterns in Marangoni convection differs qualitatively from the appearance of squares in other convective flows, where square patterns arise at the primary instability of the uniform state. For example, in buoyancy-driven (Raleigh–Bénard) convection in a binary fluid,[11,12] square patterns arise at onset and lose stability to rolls (stripes) as ΔT is increased. Squares also arise at the primary instability in pure fluid Raleigh–Bénard convection that either has a strongly temperature-dependent viscosity[13] or is sandwiched between top and bottom boundaries of poor thermal conductivity;[14] in the former case, hexagons can also occur at the onset of convection, but are observed to lose stability to either stripes[15,16] or to disordered polygons[13] that are similar in appearance to patterns arising from instability of hexagons in Marangoni convection at high P.[2]

Pattern competition between hexagons and squares in Marangoni convection poses interesting theoretical challenges similar to those that arise in pattern selection in a ferrofluid layer. In the latter case, experiments show that a steady hexagonal planform may lose stability either to stripes or square patterns.[17,18] Symmetry-breaking bifurcation theory applied to ferrofluid instability captures some features of the pattern selection,[18] but is inherently unable to describe the transition between hexagons and squares in ferrofluids or in Marangoni convection because no two-dimensional lattice can be constructed that contains the symmetries of both patterns as subgroups.[18] An additional difficulty arises when the stable wave number for the patterns may vary over a range of values (Figs. 7 and 8).[18] Model equations can be formulated where hexagons and squares may compete;[19] however, in this case, no direct connections can be made between the coefficients for the model equations and the conditions of the experiments.

An open experimental issue is the nature of instability of square patterns for M sufficiently large. Our preliminary observations indicate that squares are transformed into disordered polygonal patterns at the onset of time dependence; the cell size continually increases with increasing M. We plan to explore these phenomena in detail in future experiments.

ACKNOWLEDGMENTS

This research is supported by the NASA Office of Life and Microgravity Sciences and Applications (Grant No. NAG3-1839) and the Office of Naval Research (Grant No. N00014-89-J-1495). SJVH acknowledges support by the NASA Graduate Student Researchers Program.

[1] H. Bénard, ''Les tourbillons cellulaires dans une nappe liquide,'' Rev. Gen. Sci. Pure Appl. **11**, 1261,1309 (1900).
[2] P. Cerisier, R. Occelli, C. Pérez-García, and C. Jamond, ''Structural disorder in Bénard–Marangoni convection,'' J. Phys. (France) **48**, 569 (1987).
[3] K. Nitschke and A. Thess, ''Secondary instability in surface-tension-driven Bénard convection,'' Phys. Rev. E **52**, R5772 (1995).
[4] K. Eckert, M. Bestehorn, and A. Thess, ''Square cells in surface-tension-driven Bénard convection: experiment and theory,'' J. Fluid Mech. **356**, 155 (1998).
[5] M. Schatz and K. Howden, ''Purification of silicone oils for fluid experiments,'' Exp. Fluids **19**, 359 (1995).
[6] N. W. Ashcroft and N. D. Mermin, *Solid State Physics* (Saunders, Philadelphia, 1976), pp. 73–75.
[7] S. VanHook, M. Schatz, J. Swift, W. McCormick, and H. Swinney, ''Long-wavelength surface-tension-driven Bénard convection: experiment and theory,'' J. Fluid Mech. **345**, 45 (1997).
[8] For our experiments, we use $M_c=95.0$ at a critical wave number $q_c=2\pi/\lambda_c=1.98$ for $d=7.11\times10^{-4}$ m and $M_c=96.4$ at $q_c=2.01$ for $d=9.65\times10^{-4}$ m. The dependence of M_c and q_c on d occurs through a modified Biot number $B_q\equiv k_g q/k\,\tanh(qd_g/d)$ that is used for the linear stability analysis. We neglect small corrections to M_c due to buoyancy effects. For further details, see D. Nield, ''Surface tension and buoyancy effects in cellular convection,'' J. Fluid Mech. **19**, 341 (1964); C. Pérez-García, B. Echebarria, and M. Bestehorn, ''Thermal properties in surface-tension-driven convection,'' Phys. Rev. E **57**, 475 (1998).
[9] D. Weaire and N. Rivier, ''Soaps, cells and statistics: Random patterns in two dimensions,'' Contemp. Phys. **25**, 59 (1984).
[10] M. Bestehorn, ''Square patterns in Bénard–Marangoni convection,'' Phys. Rev. Lett. **76**, 46 (1996).
[11] P. LeGal, A. Pocheau, and V. Croquette, ''Square versus roll pattern at convective threshold,'' Phys. Rev. Lett. **54**, 2501 (1985).
[12] E. Moses and V. Steinberg, ''Competing patterns in a convective binary mixture,'' Phys. Rev. Lett. **57**, 2018 (1986).
[13] D. B. White, ''The planforms and onset of convection with a temperature-dependent viscosity,'' J. Fluid Mech. **191**, 247 (1988).
[14] P. LeGal and V. Croquette, ''Appearance of a square pattern in a Rayleigh–Bénard convection experiment,'' Phys. Fluids **31**, 3440 (1988).
[15] S. Ciliberto, E. Pampaloni, and C. Pérez-García, ''Competition between different symmetries in convective patterns,'' Phys. Rev. Lett. **61**, 979 (1988).
[16] E. Bodenschatz, J. de Bruyn, G. Ahlers, and D. Cannell, ''Transitions between patterns in thermal convection,'' Phys. Rev. Lett. **67**, 3078 (1991).
[17] A. G. Boudouvis, J. L. Puchalla, L. E. Scriven, and R. E. Rosensweig, ''Normal field instability and patterns in pools of ferrofluid,'' J. Magn. Magn. Mater. **65**, 307 (1987).
[18] M. Silber and E. Knobloch, ''Pattern selection in ferrofluids,'' Physica D **30**, 83 (1988).
[19] M. Bestehorn and C. Pérez-García, ''Study of a model of thermal convection in cylindrical containers,'' Physica D **61**, 67 (1992); C. Kubstrup, H. Herrero, and C. Pérez-García, ''Fronts between hexagons and squares in a generalized Swift–Hohenberg equation,'' Phys. Rev. E **54**, 1560 (1996).